REVIEW

Physicochemical Properties of Oriented Crystalline Assembled Polyaniline/Metal Doped $Li_4Ti_5O_{12}$ Composites for Li-ion Storage

Khaled Faisal Qasim[1] · Mahmoud Ahmed Mousa[2]

Abstract

In this work, pure, doped Mg–, Mn–, and V-$Li_4Ti_5O_{12}$, as well as polyaniline (PANI), and binary composites have been synthesized for supercapacitor applications. In situ, oxidation polymerization was used to create the nanocomposites. XRD, SEM, and XPS characterized the crystal structure, morphology, and compositions. The XRD analysis shows that all the pure and doped samples crystallize in the cubic spinel phase with a preferred orientation of the crystallites along the (111) direction, and the crystallite size has decreased with the addition of doping. The composites' SEM investigation revealed the production of LTO nanoparticles coated with PANI. The influence of dopant type on electrical and electrochemical characteristics was studied. The electrochemical performance is analyzed by cyclic voltammetry (CV), galvanostatic charge/discharge (GCD), and impedance methods in a 1 M $LiNO_3$ electrolyte solution, whereas their electrical conductivity and dielectric constant are measured by electric impedance spectroscopy. All samples showed conductivity and dielectric properties depending on the composition of the samples. The electrical conduction is enhanced by adding PANI to the pure and doped LTO samples. The electrochemical data obtained showed pseudo-capacitive behavior with a revisable charge/discharge property, and specific capacitance values lie between 58 and 202 F/g depending upon sample composition. The V-LTO@PANI demonstrates the highest performance among all the tested electrodes. The V-LTO@PANI electrode shows a specific capacitance of 202 F/g, a maximum energy density of 72.8 Wh/kg, a maximum power density of 2430 W/kg, and high cycling performance, with 82.6% capacitance retained over 3000 cycles at 1 A/g.

Keywords Self-polymerization · Spinel · Dielectric · XRD · Energy storage

1 Introduction

The production and consumption of energy today are closely linked to several environmental issues, including air pollution, climate change, water pollution, and the collection of solid refuse [1]. Among the many useful, viable options, energy can be produced electrochemically and kept in batteries and supercapacitors (SCs) [2, 3]. The charging and discharging processes used by batteries and supercapacitors, as well as the materials used to construct their components, are very distinct [4]. Because they can store a significant amount of energy in a comparatively small volume and weight and provide suitable power levels for a variety of uses, batteries are the technology of choice for the majority of users [5–7]. However, batteries have several issues including poor power density and a constrained number of charging/discharging cycles. On the other hand, supercapacitors are energy storage systems that have a high capacity and minimal internal resistance [8].

Their energy storage mechanism involves physically storing charges in an electric double layer at the interface between a surface and an electrolyte, which allows them to save and create energy at significantly higher rates than batteries. The charge condition does not significantly alter the material's structure [9]. Therefore, batteries are required for equipment with long-lasting energy needs and low power output [10]. Capacitors are recommended for applications requiring high-power energy delivery. Due to their distinct advantages over batteries, such as higher power density, long cycling life, and improved cycle stability, supercapacitors are thus seen as a more useful energy storage technology.

✉ Khaled Faisal Qasim
Khaled.Faisal@sci.suezuni.edu.eg

[1] Chemistry Department, Faculty of Science, Suez University, Suez, Egypt

[2] Chemistry Department, Faculty of Science, Benha University, Benha, Egypt

Springer

Supercapacitors can be divided into two types based on how they store charge: electric double-layer capacitors (EDLCs) or pseudocapacitors. In EDLCs, energy is stored through reversible charge collection at the electrode–electrolyte interface by fast electrolyte ion adsorption and desorption. In contrast, pseudocapacitors store energy by fast and reversed redox reactions on the electrode surface of conducting polymers or metal oxides.

Generally, in energy storage devices, the mechanism of electrochemical electrodes is detected by their physico-chemical properties, like chemical structure, particle size, crystallinity, and morphology [11, 12]. The inverse spinel-$Li_4Ti_5O_{12}$ (LTO) is one of the electrode materials that can be used for high-power energy devices. Li^+ ions take up residence in sites 8a and 16d of the original LTO crystal structure, whereas O^{2-} ions occupy sites 32e. When LTO is lithiated, the extra Li ions that were inserted occupy the octahedral 16c sites, and other Li atoms change the cubic structure's 8a to 16c vacancies. In the end, $Li_{4+x}Ti_5O_{12}$ only has all 16c sites filled at the Li content of (x = 3), indicating the creation of stable $Li_7Ti_5O_{12}$ and electron transport between Ti^{3+} and Ti^{4+}. [13].

The $Li_4Ti_5O_{12}$ spinel is a marvelous electrode due to its safety, long cycling life, high Li^+ mobility, effective Li^+ intercalation, structural stability throughout cycling, and broad temperature work range. However, low electrical conductivity ($\sigma < 10^{-13}$ S/cm) [14] and low Li-ion diffusion coefficient ((10^{-8} cm^2/s) of $Li_4Ti_5O_{12}$ significantly limit its rate performance [15] are considered a disadvantage. Nowadays, several attempts to resolve these issues, including 1-nanoscale particle preparation to decrease the Li^+ pathway and increase the diffusion coefficient [16–20]. 2- conductive phase surface covering, such as carbon-based materials coating [21]. 3- Ions doping in the Ti^{4+} or Li^+ octahedral sites [17, 22–24]. These tactics may also be used to increase LTO intrinsic conductivity [16, 25–29].

PANI is a conducting polymer for various applications, including supercapacitor applications, owing to its magnificent thermal and chemical stability, high electrical conductivity, great flexibility, cheapness, and various redox state. Although it has a high theoretical capacitance, its limited cycle stability reduced its energy storage application [30, 31].

Composite materials can be created by distributing transition metal oxides in conducting polymers. Due to the synergistic interaction of the two elements, they exhibit great surprising hybrid properties [32]. This suggests that a hybrid EDL/Faradaic pseudocapacitive material may be suitable for supercapacitor devices with a high energy density and specific capacitance [33–35].

In this work, we used a solid-state method to produce pure LTO and Mg, Mn, and V-doped LTO nanoparticles, as well as a chemical polymerization method to synthesize PANI and composites of pure and doped LTO@PANI nanoparticles. The addition of a $BaSO_4$ seed with low percent (< 5%) during polymerization gives oriented assembled PANI showing a higher AC conductivity and enhancing the capacitive parameters of PANI [36, 37]. The samples were characterized using XRD and SEM methods, and their electrical and electrochemical characteristics were examined using the electrochemical instruments EIS, CV, and GCD. How doping and surface modification affect the electrical conductivity and electrochemical properties of LTO materials has been documented and discussed. Of all the materials under investigation, the doped LTO@PANI composite had the highest specific capacitance and the best cycle life.

2 Experimental

2.1 Materials

All chemicals were reagent grade. (Li_2CO_3) 98%, (TiO_2) 98%, (C_6H_5-NH_2) 98.5%, ($K_2S_2O_8$) 98%, (MnO_2), (MgO), (V_2O_5) 99%, Poly (vinylidene fluoride) 99.5% (M.wt = 543,000 g/mole), (HCl) 35%, (C_2H_5OH) 99%, $BaCl_2.2H_2O$, and Carbon black were supplied from Alfa Aesar.

2.2 Preparation Methods

2.2.1 Preparation of Pure $Li_4Ti_5O_{12}$ (LTO) and Doped LTO (V-LTO)

Pure $Li_4Ti_5O_{12}$ (LTO) and Mn, V, Mg-doped LTO were prepared through a modified solid-state method [38]. The TiO_2: Li_2CO_3 molar ratio of 5:2.3 was used to synthesize the LTO in a stoichiometric formula of $Li_4Ti_5O_{12}$ [39]. TiO_2 and Li_2CO_3 were completely mixed with the necessary amounts of MgO, MnO_2, and V_2O_5 dopants to create samples of $Li_{3.9}Mg_{0.1}Ti_5O_{12}$, $Li_{3.9}Mn_{0.1}Ti_5O_{12}$, and $Li_{3.9}V_{0.1}Ti_5O_{12}$ as seen in Table 1. The combined powders were treated in a vigorous ball mill for a week, then autoclaved in ethanol for 24 h at 150 °C. Absolute ethanol was used to wet the particles during this process. The remaining slurry was then dried for an hour at 80 °C to remove the ethanol. LTO samples were then calcined at 750 °C in the air for two hours.

2.2.2 Preparation of Polyaniline Composites (LTO@PANI)

PANI composites were prepared by in-situ oxidation-polymerization [37]. In the standard processes, aniline hydrochloride was created by ultrasonically combining 1 g of the produced LTO (pure or doped) with 2 ml of aniline monomer dissolved in 100 ml of 1 M HCl, and 0.01 g of $BaCl_2.6H_2O$ was added during the sonication process. $K_2S_2O_8$ was used

Table 1 Stoichiometric ratios of the prepared materials

Sample	Molar ratio (Mole)			Mass ratio (g)		
	Li	Ti	Doping	Li	Ti	Doping
LTO	4.6	5	–	1.69	3.99	–
Mg-LTO	4.5	5	0.1	16.6	3.99	0.04
Mn-LTO	4.5	5	0.1	16.6	3.99	0.086
V-LTO	4.5	5	0.1	16.6	3.99	0.09

as the oxidant, and 50 ml of 0.1 M was carefully added while continuously stirring for three hours in an ice bath. To remove any extra oxidant and unreacted monomers, the solution was washed with 250 ml of distilled water after being left in the solution for 24 h to finish polymerization. Finally, the produced polymer was filtered and dried in air at 60 °C to get a consistent weight.

2.3 Materials Characterizations and Measurements

Cu-K with $\lambda = 0.154$ nm and a diffraction angle between 15 and 80º was used in an X-ray diffractometer (Philips XL 40) to record the XRD patterns of the materials. The morphology of the materials was analyzed with a scanning electron microscope (SEM) (JEOL-JSM-6510 LV). Rietveld refinement approach was used to confirm the crystalline structures of LTO and doped LTO samples, employing the GSAS program with the EXPGUI interface. X-ray Photoelectron Spectroscopy (XPS) studies were performed using a KRATOS XSAM-800 and calibrated by adventitious carbon.

2.3.1 Electrochemical and Dielectrics Measurements

2.3.1.1 Preparation of Working Electrodes To make the electrodes, a paste was made by blending LTO materials, carbon black, polyvinylidene fluoride in the proportions 75:15:10, and a few drops of ethanol. The paste was created on FTO glass using the doctor blade method and allowed to dry at 80 °C for two hours to evaporate the solvent for the optimum adhesion to the substrate surface.

2.3.1.2 Electrochemical and Electrical Measurements Cyclic voltammetry (CV) and galvanostatic charge–discharge (GCD) techniques were used using the Digi-Ivy 2116 B instrument to determine the studied electrodes' energy storage capacity. EIS was measured by (Metrohm Auto Lab PGSTAT 204), Netherlands, between 0.1 Hz and 100 kHz at a constant voltage of 10 mV. A cell with three electrodes was used to determine the electrochemical characteristics in a published worldwide. The examined materials were used to make working electrodes on FTO glass, whereas the reference and counter electrodes were saturated

calomel electrodes (SCE), Pt foil, and 1 M $LiNO_3$ aqueous solution, respectively. CVs were run between − 1.1 and 1.1 V at scan rates between 1 and 100 mV/s. GCD was measured between 0.5 and 3 A/g of current density. GW Instek 8110G LCR meter, Taiwan, was used to measure the dielectric properties of AC conductivity (AC), dielectric constant, and dielectric loss across the frequency range of 10^3–10^7 Hz. Samples were pressed as pellets, then connected to a 4-port LCR bridge via a conductive cell.

## 3 Results and Discussions

3.1 Chemical Characterizations

Figure 1a shows the XRD patterns of the pure and doped LTO samples. The diffraction peaks for the pure LTO sample are at 2θ = 18°, 37°, 43°,49°, 58°, 63°, 66°, 75°, 76°, and 79°, corresponding to (111), (311), (400), (331), (511), (440), (531), (532), (622), (444) planes, respectively. They correspond to the LTO cubic spinel phase structure (JCPDS card no. 49–0207). The spinel structure was also seen in the XRD of the LTO-doped samples. All of the observed diffraction peaks have indicated the formation of pure and highly crystalline LTO materials. Additionally, it was noted that the introduction of dopant ions into the LTO lattice caused the diffraction peak of the (111) crystal plan to move noticeably to the right. This shift is due to the presence of atoms with smaller substituted ionic radii (The ionic radius of Mg^{2+}, Mn^{4+}, and V^{5+} are 72, 53, and 46 pm), which are smaller than Ti^{4+} and Li^+ (60 pm) [40, 41]. These results suggest that the dopant was effectively generated in the (111) plane of $Li_4Ti_5O_{12}$'s spinel lattice. In conclusion, The XRD results confirm no modification in the structure but a change in the cubic parameter.

The XRD of the LTO@PANI composites, as shown in Fig. 1b, displays peaks associated with the orthorhombic phase structure of $BaSO_4$ in addition to the peaks of the LTO spinel structure. The peaks of the orthorhombic structure of $BaSO_4$ appeared at 2θ = 20.6°, 22.8°, 25°, 25.9°, 27°, 28.8°, 31.7°, and 32.8° corresponding to (011), (111), (002), (210),
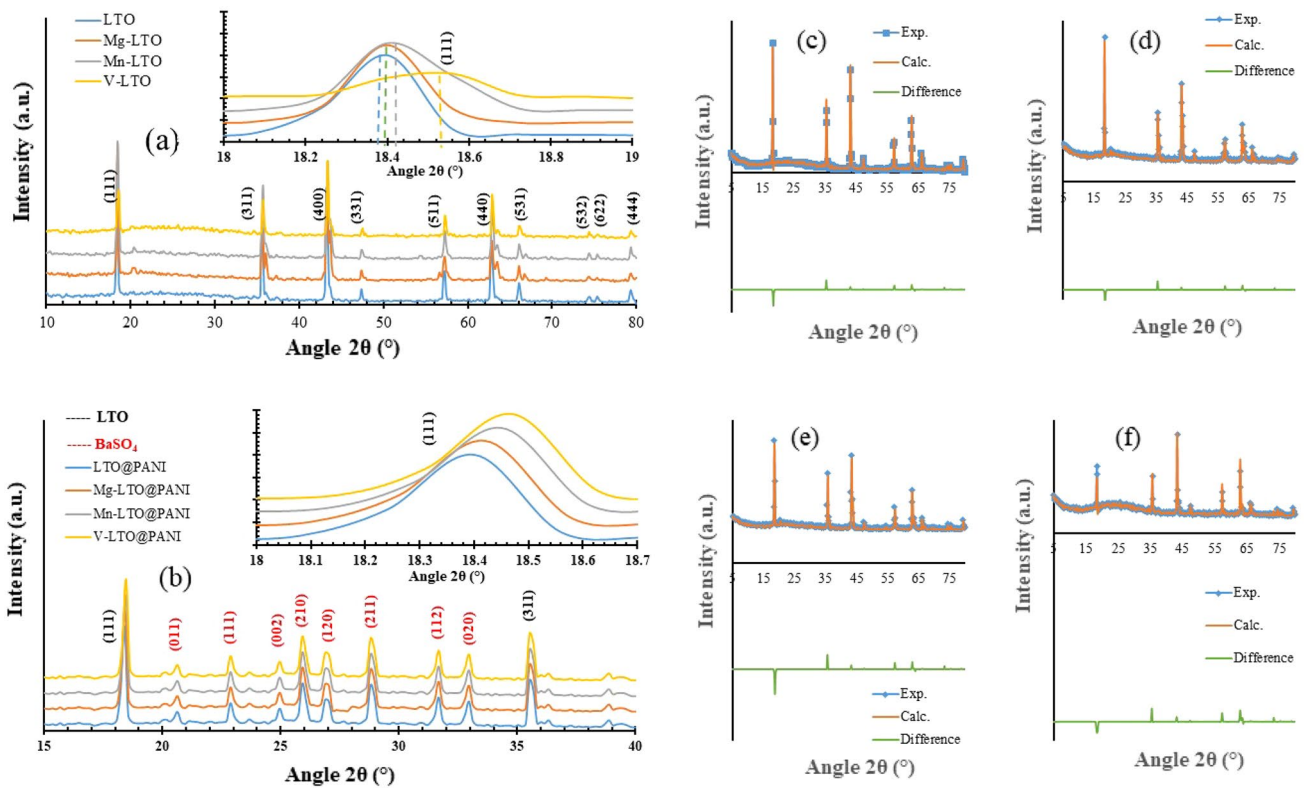
Fig. 1 XRD of **a** LTO samples, **b** LTO@PANI samples, Rietveld Refinement of **c** LTO, **d** Mg-LTO, **e** Mn-LTO, **f** V-LTO

(120), (211), (112), and (020) planes, respectively,(JCPDS No. 24–1035) [39, 42], The BaSO$_4$ was formed during the polymerization of PANI, as shown in the following equation [37].
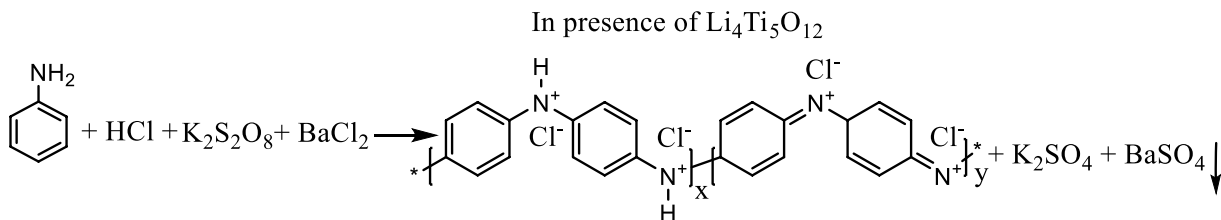
The presence of BaSO$_4$ planes on XRD occurred because of the oriented assembling of PANI on the surface of BaSO$_4$ seed owing to the similarity of crystal structure between PANI and BaSO$_4$ [36].

The XRD reveals the presence of some interactions between LTO and PANI in the composite samples, as seen by the small changes in the peak locations of LTO in the

LTO@PANI composite samples compared to those seen for the pure LTO [36].

The texture coefficient (T_c) was derived from XRD data using Eq. 1 [43] to identify the relative degree of preferred orientation among crystal planes of examined materials.

$$T_c(hkl) = \frac{\frac{I(hkl)}{I_o(hkl)}}{\frac{1}{N}\sum_N \frac{I(hkl)}{I_o(hkl)}} \quad (1)$$

where (hkl) are the Miller indices, I(hkl) is the measured intensity of X-ray reflection, Io (hkl) is the equivalent standard intensity from the JCPDS card (49–0207), and N is the number of reflections seen in the XRD pattern. The variation

Table 2 Surface and structural data of samples

Sample	SSA (m²/g)	Vp (cm³/g)	T_C (max)	plan	Williamson-Hall			Scherer Debye			Lattice Parameter	
					D (nm)	δ (line/m²)	ε (×10⁻⁴)	D (nm)	δ (line/m²)	ε (×10⁻⁴)	a (Å)	V (Å³)
LTO	30.7	9.58×10^{-3}	2.59	(111)	40.7	4.35×10^{14}	5.1	36.5	7.5×10^{14}	8.8	8.342	580.6
Mg-LTO	40.1	1.16×10^{-2}	2.18	(111)	40.1	4.95×10^{14}	3.8	36.2	7.63×10^{14}	5.1	8.348	581.8
Mn-LTO	38.9	1.14×10^{-2}	2.07	(111)	39.8	4.87×10^{14}	2.9	35.9	7.76×10^{14}	4.3	8.334	578.9
V-LTO	31.1	9.92×10^{-3}	2.00	(400)	39.5	1.45×10^{15}	2.6	35.6	7.9×10^{14}	4.1	8.331	578.2
LTO @PANI	56.4	3.05×10^{-2}	1.57	(111)	40.2	6.42×10^{14}	5.6	32.4	7.9×10^{14}	9.1	8.34	580.1
Mg-LTO@PANI	57.1	3.64×10^{-2}	1.42	(111)	39.7	7.1×10^{14}	4.1	32	8.2×10^{14}	7.3	8.345	581.13
Mn-LTO@PANI	58.3	3.97×10^{-2}	1.31	(111)	38.9	8.6×10^{14}	3.3	31.8	8.8×10^{14}	6.5	8.3	571.8
V-LTO@PANI	58.8	4.03×10^{-2}	1.27	(400)	38.4	1.9×10^{15}	2.9	31.2	9.4×10^{14}	5.2	8.328	577.6

in Tc with 2θ for different hkl values is listed in Table 2. The more excellent T_c value refers to the abundance of grains oriented along a given hkl plane. Table 2 shows that the greatest Tc values were observed for plans (111) and (400), indicating that the crystallites were more oriented along these planes.

Because $Li_4Ti_5O_{12}$ exhibits a face-centered cubic structure, the lattice constant (a) is computed by using lattice space d_{hkl} using Eq. (2) [44]

$$d_{hkl} = a/\sqrt{(h^2 + k^2 + l^2)} \qquad (2)$$

The results obtained are also listed in Table 2, which shows a decrease in the lattice parameter (a) of all doped materials, except that containing Mg, compared with that of pure LTO. Because Mg^{2+}'s ionic radius (72 pm) is larger than Li^+ (60 pm), Mg ions were easily incorporated into the Li sites of the Mg-doped LTO. This substitution can promote the reduction of Ti^{4+} to Ti^{3+} to balance the charge [29]. This may be the reason for the increase in the lattice constant parameter of the Mg-LTO specimen because the ionic radius of Ti^{3+} (67 pm) is larger than that of Ti^{4+} (60 pm) [41].

The average crystallite size of the investigated samples was calculated using two different equations (Scherrer-Debye Eq. (3) and Williamson-Hall Eq. (4)) [44]

$$D = \frac{0.9\lambda}{\beta \cos\theta} \qquad (3)$$

$$\beta_{hkl} \cos\theta = \frac{K\lambda}{D} + 4\varepsilon\sin\theta \qquad (4)$$

where λ is the X-ray wavelength employed, and β denotes full width of half maximum peak (FWHM). The results obtained are also reported in Table 2, which illustrates that all the samples lie on the nanometer scale and that their sizes decrease by adding dopants.

The strain (ε) induced in the samples was calculated using Eqs. (5, 6) [45]

$$\beta_s = 4\varepsilon\tan\theta \qquad (5)$$

$$\varepsilon = \frac{\beta\cos\theta}{4} \qquad (6)$$

The results are listed in Table 2, which shows an increase in the strain of the pure LTO due to the addition of dopants. This is explained by the fact that dopant ionic radii are lower than Ti^{4+} (60 pm) and Li^+ (68 pm), hence replacing Ti^{4+} or Li^+ ions with Mg^{2+}, Mn^{4+}, and V^{5+} ions will enhance the strain of LTO crystals [46]. Dopant addition increases strain because the Lattice constant decreases as compared to pure LTO. That is, the dopant causes mechanical strain on the lattice's surface, causing it to shrink.

The dislocation density (ρ_D), which denotes the number of defects in the prepared materials, defines the length of the dislocation line per unit volume of the crystals and is calculated by using the Eqs. (7, 8) [43]

$$\rho_D = \frac{1}{D^2} \tag{7}$$

$$\rho_D = \frac{15\,\varepsilon}{a\,D} \tag{8}$$

The results obtained are given in Table 2, which shows that the addition of dopants leads to a change in ρ_D value due to the dissimilarity of either ionic radii or valency charges between the substituted dopants (Mg, Mn, V) and the host elements (Li, Ti). That increases the bulk deformation of crystals [46], and in turn, the ρ_D value increases.

To identify the nature of the doping site in the LTO Fd-3 m lattice, Rietveld refinement of the synchrotron X-ray diffraction data for the studied samples was performed. The Rietveld patterns for pure and doped materials were shown in Fig. 1c–f and compared to the experimental patterns. The acquired outcomes from a model with Li1 atoms in the 8a (1/8, 1/8, 1/8) position, Li2/Ti atoms in the 16d (1/2, 1/2, 1/2), and O atoms in the 32e (x, x, x) position are enumerated in Table 3, which displays good values for profile (R_p), weighted profile residuals (R_{wp}), and goodness of fit (χ^2). However, some significant structural changes occurred across the doped LTO and pure LTO samples. The oxygen coordinate (x), the lattice parameter (a), the lattice volume (V), the Li1-O bond distance, and the Li1-Li1 bond distance are all less in the doped LTO samples, although the Li2/Ti–O bond distance is bigger. These variations indicate that both the pure and doped LTO include larger tetrahedrons and smaller octahedrons. The number of accessible octahedral cavities determined the Li-insertion capacity [47], and the low value of x implied structural distortion [20]. As a result, when Li-ion diffuses in the < 111 > direction, the doped LTO

Table 3 Rietveld mathematical data of the pure and doped LTO samples

Sample	a (Å)	V (Å³)	x'	Li1-O	Li2/Ti–O	Li1-Li1	R_p (%)	R_{wp} (%)	χ^2
LTO	8.361	584.487	0.2617	1.9734	1.9958	3.6206	6.11	7.73	2.223
Mg-LTO	8.366	585.536	0.2587	1.9362	2.0186	3.619	7.41	9.55	2.615
Mn-LTO	8.348	581.7646	0.2563	1.9276	2.0268	3.619	7.83	8.46	2.557
V-LTO	8.336	579.259	0.2554	1.9023	2.0342	3.617	8.32	8.56	2.625
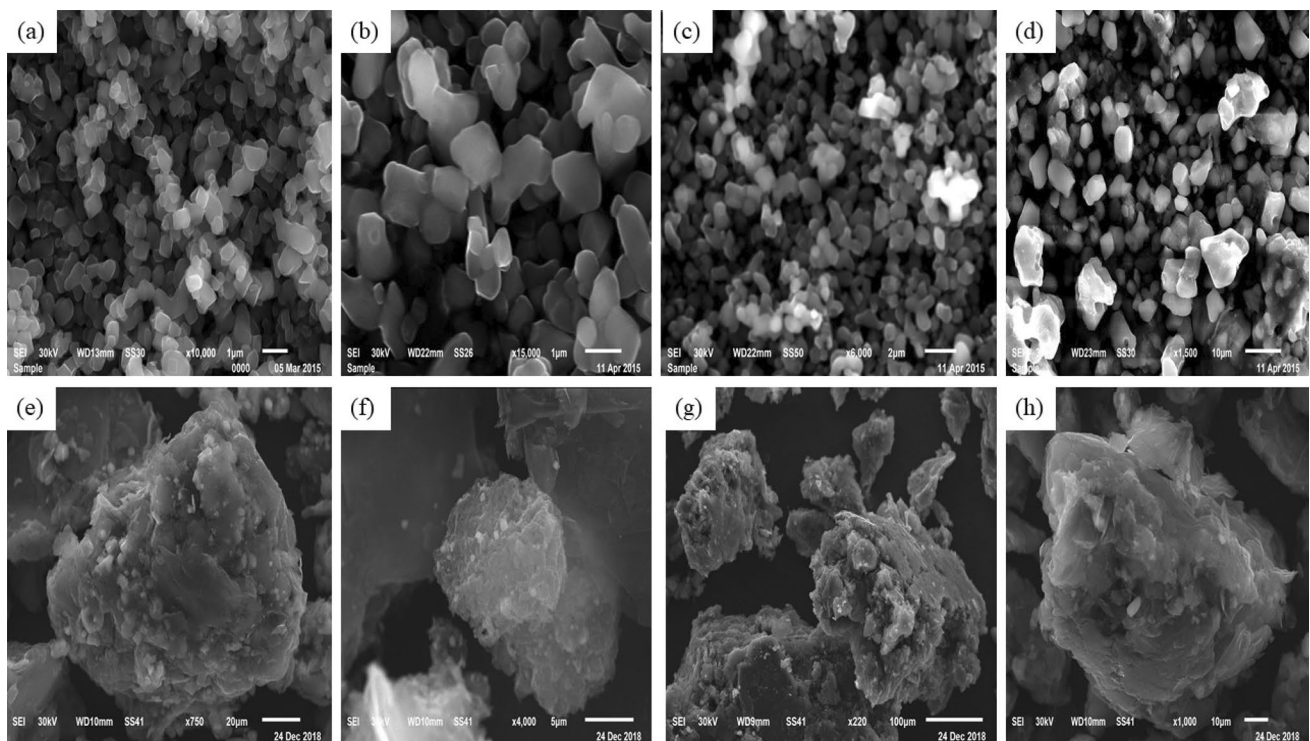
Fig. 2 SEM of **a** LTO, **b** Mg-LTO, **c** Mn-LTO, **d** V-LTO, **e** LTO@PANI, **f** Mg-LTO@PANI, **g** Mn-LTO@PANI, **h** V-LTO@PANI,

electrode is anticipated to perform electrochemically better than the LTO electrode.

The SEM micrographs of the investigated samples are given in Fig. 2a–h. The images of the pure and doped LTO, Fig. 2a–d, illustrate a cubic morphology with an average length of 0.08–0.15 μm, distorted by dopants addition. The SEM images of the composite samples, Fig. 2e–h, show core–shell structures of the pure and doped LTO as cores wrapped in polymer matrix shells that form agglomerates of 50–80 μm. The agglomerates are due to polymer matrix formation, which makes a core–shell structure beside the metal bridge with polymer skeletons that increase polymer stacking on the surface of LTO. The agglomerated particles in the composites form different domains for conducting and insulating areas, influencing the electrical characteristics as seen in our conductivity data.

As shown later, the electrochemical performance and dielectric studies demonstrated that binary systems offer better behaviors than pure ones. This might be connected to the kind of bonds and valence state fluctuation in doped binary materials, which can be studied using the XPS method. The results obtained are shown in Fig. 3. The scanner spectrum shows that the sample contains only the main elements: Ti, O, Mn, V, and N. The high-resolution XPS spectra of Mn ($2p^{3/2}$), Ti ($2p^{3/2}$), N (1 s), O (1 s), and V($2p^{3/2}$) peaks. Ti ($2p^{3/2}$) bands are observed at 455.2 eV and 456.5 eV are

assigned for Ti^{+2} ($2p^{1/2}$) level, and Ti^{+3} ($2p^{3/2}$) level, respectively, it's also observed 2 peaks at 457.7, and 458.8 which they are related to Ti^{+4}-O ($2p^{1/2}$) level, and O-Ti^{+4}-N ($2p^{3/2}$) level, respectively [48]. V ($2p^{3/2}$) spectrum shows 4 peaks with binding energies of 513.7, 514.4, 516.3, and 517.8 eV which are related to V^{+2}, V^{+3}, V^{+4}, and V^{+5}, respectively [49–53], and referring to the presence of various oxidation states of V ion. This might be attributed to the reduction of V$^{+5} \rightarrow$ V$^{+4} \rightarrow$ V$^{+3} \rightarrow$ V^{+2} during the polymerization process of PANI. Mn ($2p^{3/2}$) spectrum shows 3 peaks at 640.6, 641.7, 642, and 644.9 eV related to Mn^{+2}, Mn^{+3}, Mn^{+4}, and Mn–N [54], which is attributed to reduction of Mn$^{+4} \rightarrow$ Mn$^{+3} \rightarrow$ Mn^{+2} during the polymerization process of PANI. These results refer to the formation of different interaction types between individual components in binary composite samples [55]. XPS of N (1 s) peaks illustrate peaks at 397.9, 398.4, 399, 399.8 400.6, and 401.8 eV referring to N–M–N, C=N, –NH, M–N$^+$H, –NH$^{+\bullet}$–and –N$^+$H (M is Mn, Ti, and/or V). The probability of M bridging is V and Mn due to their oxidative property which helps the formation of N–M–N, which proves that N has various bonding arrangements [24, 56, 57] [58]. O(1 s) shows peaks at 530.8 eV, 532, 532.9 eV, and 535.3 eV related to Ti–O, M–O, M–OH, and H$_2$O respectively [48, 50, 59].

For further consideration of surface parameters to illustrate the electrochemical performance of the prepared
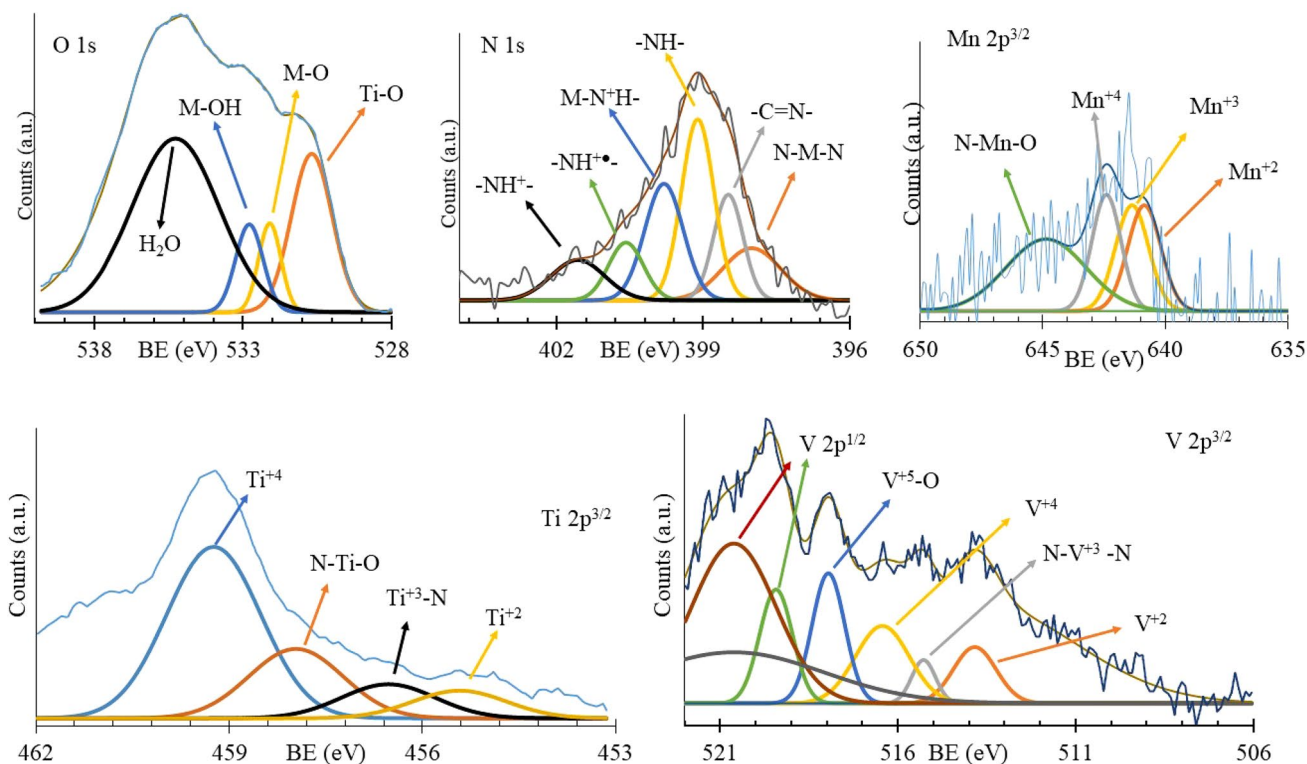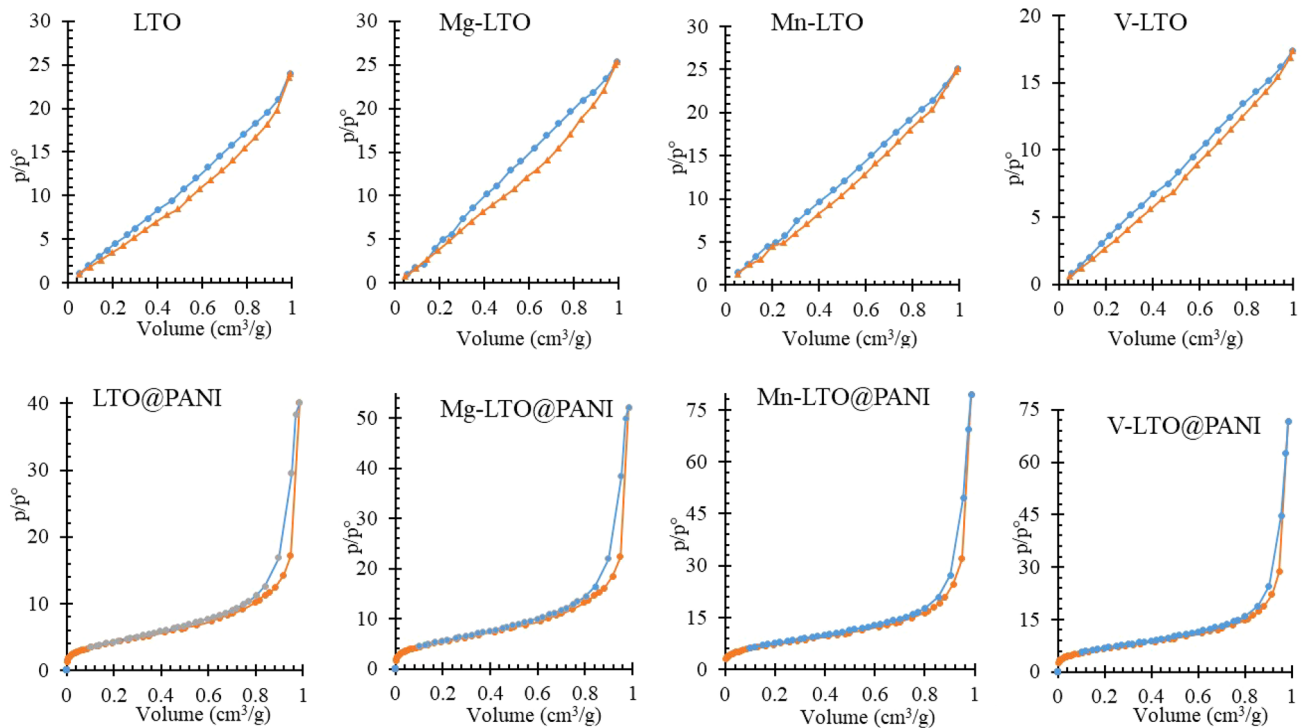

Fig. 3 XPS of elements in LTO@PANI samples

Fig. 4 N$_2$ Adsorption/desorption isotherm of the prepared samples

samples (LTO samples and their composites), N$_2$ adsorption–desorption isotherms are studied and revealed in Fig. 4.The isotherm of LTO samples is classified (according to IUPAC classification) as Type IV isotherms with hysteresis loops, which shows the mesoporous nature of the material. Adding a dopant doesn't change the isotherm type, but variation happens in surface parameters like specific surface area (SSA) and pore volume (V$_p$). The addition of PANI in composite samples improves surface characteristics due to chemical composition branching, which increases the pores and active sites in the binary system structure. The results are listed in Table 2.

3.2 Electrical Studies

The results of analyzing pure and doped LTO, PANI, and their composites for AC conductivity at room temperature and frequencies between 10^3 and 10^7 Hz are displayed in Fig. 5. For all samples, the AC increases almost linearly with frequencies up to 5×10^5 Hz. At this point, it rises sharply in the following order: LTO > Mn-LTO > Mg-LTO > V-LTO.

The results further showed that at all applied frequencies, the AC values of LTO were greater than those of doped LTO. This could be explained by the fact that the electronic charge transfers in the doped LTO lattice will be more diffused in the doped LTO lattice because doped LTO samples have lower lattice constants than LTO [60].

The conductivity studies further demonstrated that the PANI addition to the LTO materials causes an increase in the σ_{ac}. This may be attributed to the formation of additional interfacial phases in the binary system [61], which leads to a rise in the polarization of samples in following order: LTO < Mg-LTO < V-LTO < Mn-LTO. The formation of the M–N bond during in-situ polymerization by the chemical interaction between LTO and PANI may also explain the increase in conductivity in binary systems. The new M–N bonds aid in electrical conductivity through the highly branched polymer matrix via -bond resonance [53]. As seen in the PANI composite diagram and validated by XPS data, the addition of PANI as a conducting polymer is dependent on the π–π* transition, which forms a bridge between the two polymer skeletons via a metal-N connection [63]. Furthermore, the inclusion of BaCl$_2$ during the polymerization process causes BaSO$_4$ seed formation, which assembles PANI on its surface and promotes the stacking of polymer layers, resulting in the facilitation of charge transfer between LTO and a polymer shell. As a result, conductivity rises. Table 4 displays the acquired results.
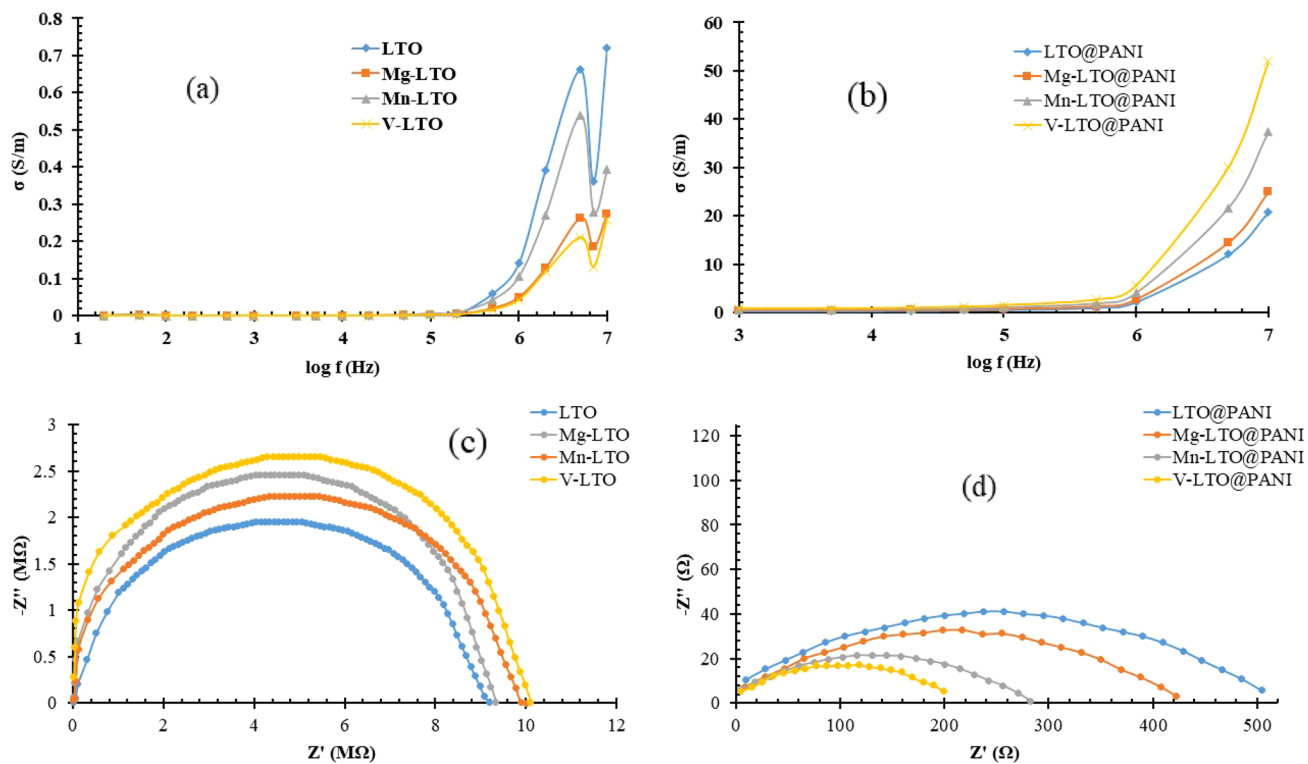
Fig. 5 AC conductivity of **a** LTO samples, **b** LTO binary samples, EIS of **c** LTO samples, **d** LTO binary samples

Table 4 Frequency effect on dielectric properties of the investigated materials

| Sample	1000 Hz			500 kHz			10 MHz			R_b (Ω)
	σ (S/m)	ε'	ε''	σ (S/m)	ε'	ε''	σ (S/m)	ε'	ε''	
LTO	6.6×10^{-5}	95	600	0.06	2.74	1.1	0.72	1.98	0.03	9.1×10^6
Mg-LTO	4.2×10^{-5}	64	195	0.019	1.36	0.6	0.19	1.1	0.12	9.3×10^6
Mn-LTO	4.7×10^{-5}	236	236	0.04	1.3	0.4	0.39	1.2	0.15	9.8×10^6
V-LTO	3.9×10^{-5}	96	165	7×10^{-4}	3.62	1.2	0.26	1.96	0.04	10.1×10^6
LTO @PANI	0.32	9.2×10^6	6.1×10^{11}	1.03	5.4×10^3	4.6×10^4	20.74	3086	1167	493
Mg-LTO@PANI	0.38	2.3×10^9	1.5×10^{13}	1.24	1.4×10^6	1.1×10^6	24.9	7.9×10^4	2.9×10^4	422
Mn-LTO@PANI	0.58	3.3×10^9	2.2×10^{13}	1.86	1.9×10^6	1.6×10^7	37.4	8.9×10^4	3.8×10^4	283
V-LTO@PANI	0.8	3.7×10^9	2.5×10^{13}	2.6	2.2×10^6	1.8×10^7	51.9	1.3×10^5	4.7×10^4	202
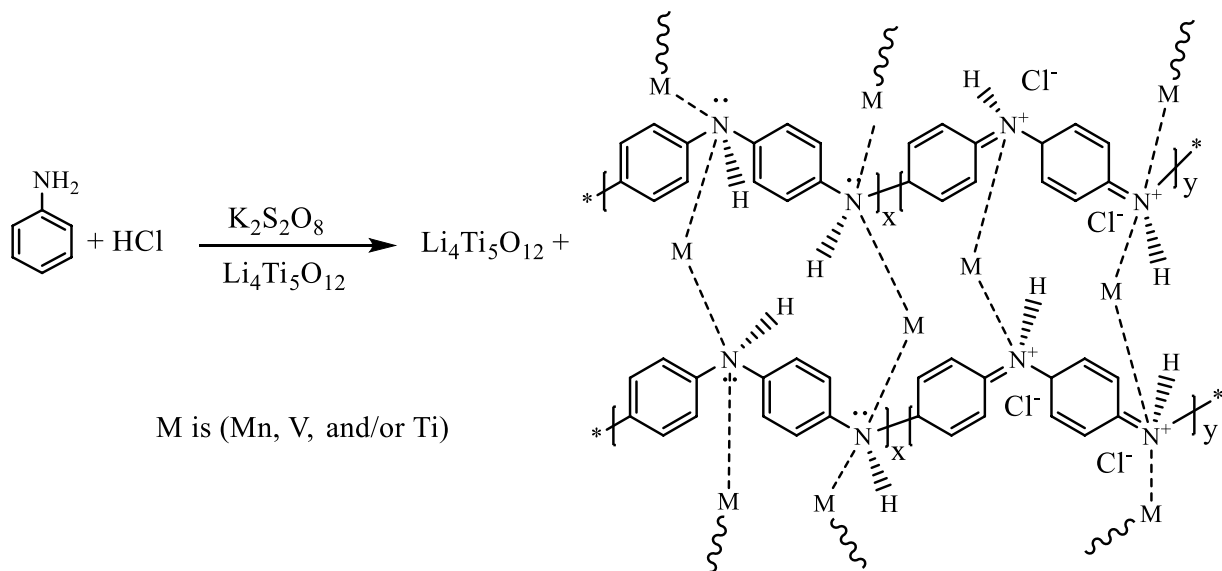
Figure 6 depicts the frequency impact on dielectric loss (ε''), and dielectric constant (ε') for the studied materials. In the low-frequency domain, ε' and ε'' values rapidly decrease with rising frequency for all samples, and at higher frequencies, they nearly adopt a frequency-independent pattern. This was explained because dipole polarization decreases when the electric field reaches higher frequencies [64].

In other words, interfaces with significant volume fractions in nanostructured dielectric materials contain many defects, including vacancies, dangling bonds, and micro-porosities. After an electric field is applied, space charges move, and when imperfections catch them, multiple dipole
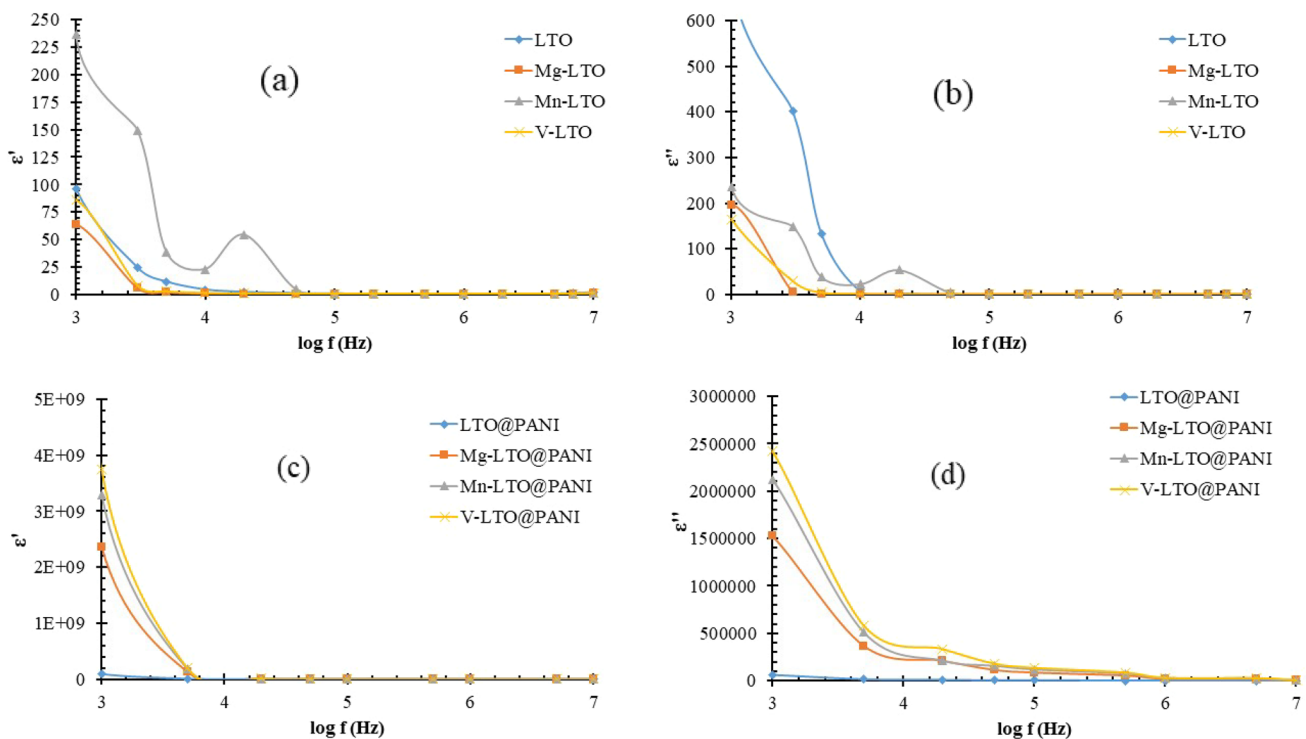

Fig. 6 Dielectric studies of investigated samples

moments are created [65]. These dipole moments ease tracking changes in the electric field at lower frequencies. The ε'- and ε''- values are consequently noticeably high at low frequencies, as seen in Table 4.

The electrical characteristics of the samples under investigation were further explored using electrical impedance (EI) measurements at frequencies ranging from 10^3 to 10^7 Hz. The acquired data are represented as a Cole–Cole diagram in Fig. 5. The plots show a single semicircular form as it approaches the origin. This pattern reveals a parallel grain boundary capacitance and resistance in the materials. It's important to observe that each arc's center is quite close to the true axis, meaning that the dispersion angle is essentially nonexistent [66, 67]. Since the semicircle centers of the composites are so close to the actual axis, it is plausible that the composite is electrically homogeneous. An overview of the EIS data that were collected for all samples is shown in Table 4. This shows how the bulk resistance increases in the following order: LTO < Mg-LTO < Mn-LTO < V-LTO. However, after combining the LTO materials with PANI, and due to the highly-branched polymer matrix structure, the R_{ct} order of PANI composites increases in the following order: V-LTO < Mn-LTO < Mg-LTO < LTO.

3.3 Electrochemical Studies

CV is a suitable method for illustrating various capacitive mechanisms kinds. Figure 7 shows the CV of the constructed electrodes at a scanning rate of 10 mV/s. The CV plots show the electrochemical behavior of pure and doped LTO samples as well as their composites. The oxidation and reduction of active sites at the electrodes result in the redox peaks visible in the plots [68, 69].

On the CV of the LTO electrode, redox peaks at -0.08 V and -0.2 V demonstrate $Ti^{4+} \leftrightarrow Ti^{3+}$ process (Fig. 7). [70, 71]. There's also a plateau at -0.7 V, which might have formed as a result of Li hopping in the LTO crystal structure [72]. Doped LTO has slightly shifted redox peaks that are equivalent to those of LTO. Mg-LTO has a slight redox peak at -0.33 V, and -0.37 V, which indicates the $Ti^{+3} \leftrightarrow Ti^{+2}$ process.

The LES $\leftrightarrow$ ES $\leftrightarrow$ PRG transformations are responsible for the redox peaks in the CV of LTO@PANI composites [73, 74]. Due to the LES $\leftrightarrow$ ES $\leftrightarrow$ PRG conversions, PANI@LTO samples displayed two redox peaks at -0.85 V and -0.64 V, respectively [73, 74]. Besides, decreased peaks corresponding to PRG $\leftrightarrow$ ES $\leftrightarrow$ LES occurred at $+0.45$ V and -0.05 V. The doped LTO@PANI composite's cyclic voltammograms, shown in Fig. 7, show the same LTO of $Ti^{4+} \leftrightarrow Ti^{3+}$ process peaks as before with a little shift of around 0.01 V, which is explained by a change in the composite's structure brought on by LTO and PANI interaction. Despite the presence of $BaSO_4$ in our samples, as demonstrated by XRD data, the typical peaks for $BaSO_4$ were not visible in the CV plots. This is because $BaSO_4$ was employed as a seed for PANI crystallization, and its concentration in the samples is too low (<2 wt%) to be detected in electrochemical experiments, especially when $BaSO_4$ peaks conflict with PANI redox peaks [36]. Using CV data and Eq. (9), the
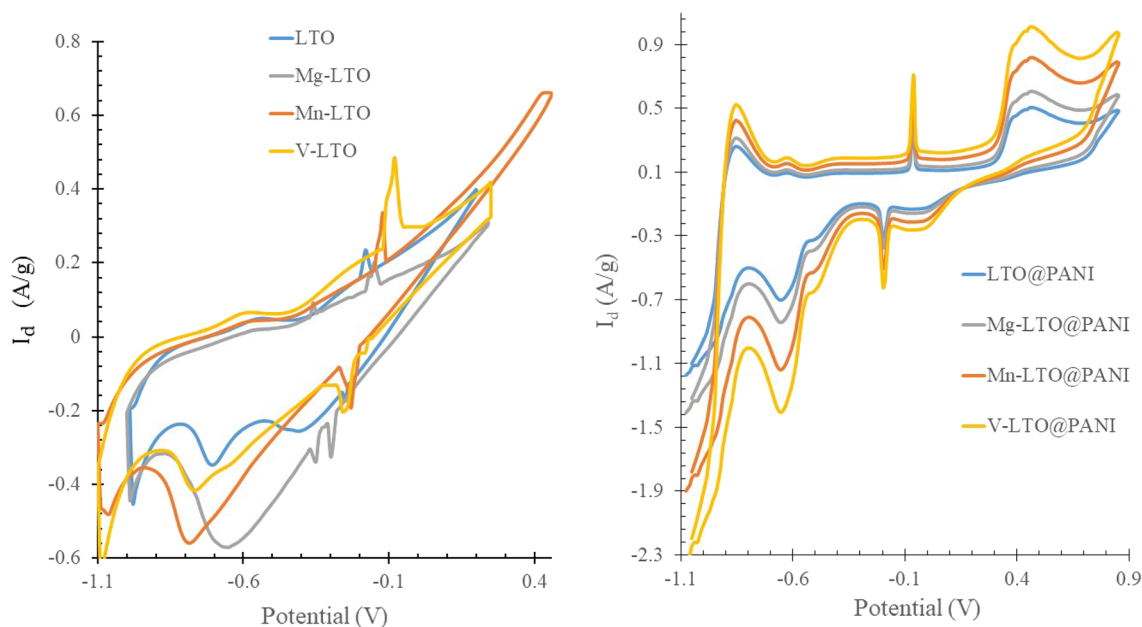

Fig. 7 CV of the investigated samples

Table 5 Electrochemical capacitive data of the investigated materials

Sample	C_{sp} (F/g) 1 mV/s	C_{sp} (F/g) 0.5 A/g	Stability 3000 cycles (%)	E_d (Wh/g)	P_d (W/kg)	W_D (Ω)	τ (ms)	R_S (Ω)	R_{ct} (Ω)
LTO	70	58	79.7	11.6	1140	239	2.6	9.2	229.8
Mg-LTO	82	62	79.9	12.4	1210	222	2.7	9.6	212.4
Mn-LTO	94	71	80.2	14.2	1320	204	2.8	10.3	193.7
V-LTO	98	80	80.5	18.8	1410	184	3.0	10.6	173.4
LTO @PANI	158	133	81.5	59.9	2160	38	1.2	16.3	21.7
Mg-LTO@PANI	177	154	81.9	63.3	2240	37	1.3	17.6	19.4
Mn-LTO@PANI	194	167	82.3	69.1	2350	30.3	1.5	16.4	13.9
V-LTO@PANI	218	202	82.6	72.8	2430	27.6	1.6	14.6	13

specific capacitance (C_{sp}) values of all the electrodes under investigation were determined [75], and given in Table 5.

$$C_{sp} = \frac{1}{m \, \nu \, V} \int_{-V}^{+V} IV \, \partial V \qquad (9)$$

where I denote current, ΔV denotes applied potential, ν denotes scan rate, and m is the active material's mass.

To more thoroughly analyze the capacitive behavior, the b value was determined using a power law using Eq. (10) [76]

$$I_m = a \, \nu^b \qquad (10)$$

where I_m is the highest current density in CV plots, and a as well as b are constant parameters. The power law relationship (Eq. 11), which describes normal battery behavior, states that the b value is generally equal to 1.0 for non-diffusion-controlled surface capacitive and 0.5 for diffusion-controlled redox reaction. According to the studied samples, the b values for pure, Mg–, Mn–, and V-LTO samples at Ti^{4+}/Ti^{3+} (− 0.08 V, and − 0.2 V) redox are found to be 0.50, 0.52, 0.54, and 0.55, respectively. That indicates the battery-type property [70]. On the other hand, the b values of composite systems at Ti^{+4}/Ti^{+3} (~ − 0.05 V, and − 0.19 V) redox are 0.72, 0.76, 0.81, 0.84 for pure, Mg–, Mn–, V-LTO
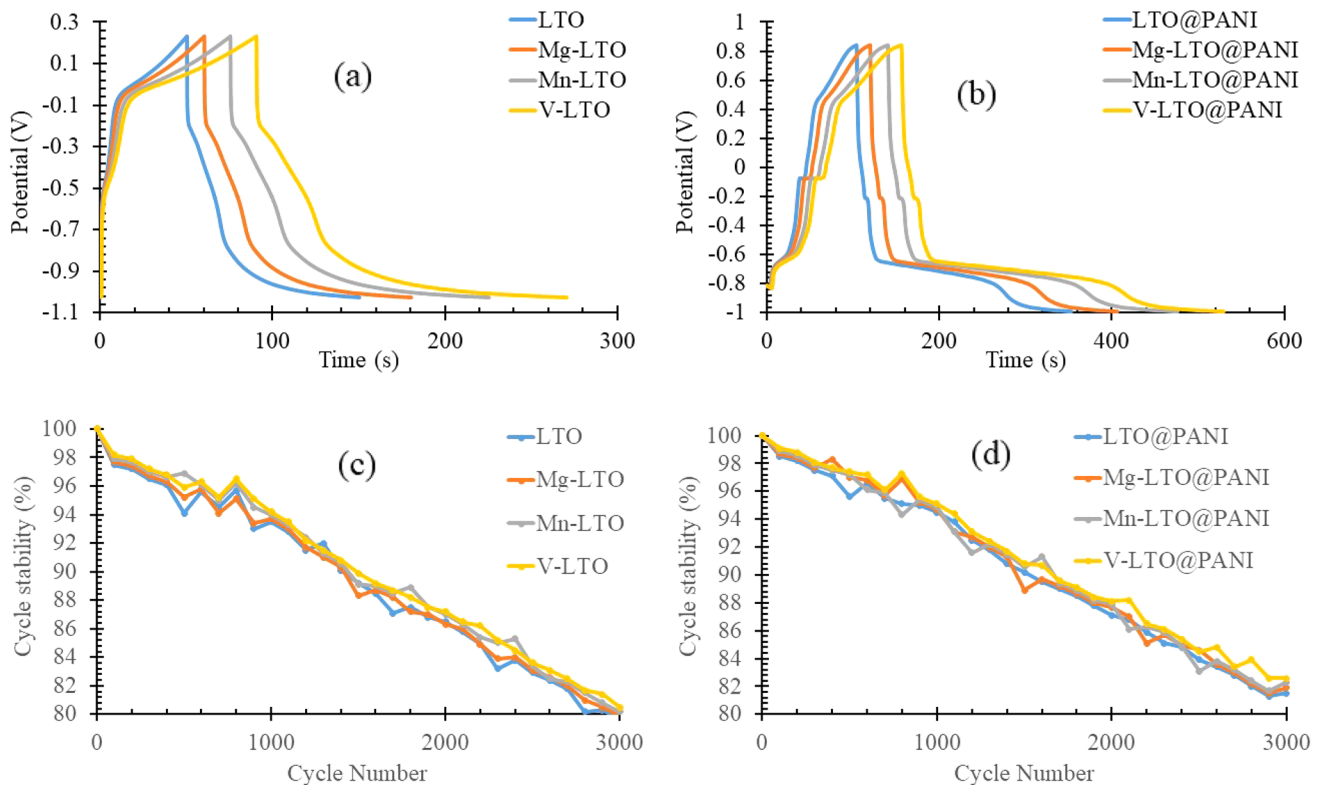
Fig. 8 GCD of the investigated samples

samples respectively. This indicates that the hybrid system performs the battery-supercapacitor hybrid mechanism [77].

Galvanostatic charge–discharge (GCD) is an equivalent technique for determining the C_{sp} of electrochemical capacitors at a constant current. Consquentl, the electrochemical behavior of the electrodes at a current density of 1 A/g was examined using the GCD method. The results are presented in Fig. 8. All discharge plots displayed an internal resistance drop (IR-drop) known as the equivalent series resistance (ESR), which includes all the resistances of the cell (electrode, electrolyte, contact resistance). The specific capacitance values C_{sp} of the electrodes were evaluated from the discharge cycles by using Eq. (11) [62].

$$C_{sp} = \frac{I \, \Delta t}{m \, \Delta V} \qquad (11)$$

where Δt is the discharge time, and ΔV is the potential range during the charge–discharge measurement. Table 5 exhibits the results and capacity enhancements for LTO samples in either single or binary composite systems in the following sequential manner: Mn-LTO > Mg-LTO > LTO > V-LTO. These are consistent with what was gained from the results of the CV. The V-LTO has a higher capacitance than LTO because of its smaller particle size and a broader electrode/electrolyte contact surface, which shortens the Li-ion route and speeds up Li-ion diffusion [62]. Furthermore, a decline

in internal resistance (IR) denotes a decline in electrode resistance [61].

The supercapacitor device's energy density (E_d) and average power density (P_d) are two important parameters. They are calculated for the composite systems that exhibit higher capacitances using Eqs. (12,13) [63]

$$E_d = \frac{1}{2} C_{sp} \Delta V^2 \qquad (12)$$

$$P_d = \frac{E_d}{t} \qquad (13)$$

The results are listed in Table 5.

Long cycling stability is an important parameter for supercapacitor operations. Thus, the electrochemical stability of the examined electrodes was investigated, at a current density of 1 A/g. The results are displayed in Fig. 8 and summarized in Table 5, which reveals that the samples have excellent cycling performance, with 79.7–82.6% capacitance preserved after 3000 cycles.

Figure 9 displays the Nyquist plots for the studied electrodes over the frequency range of 10^{-2}-10^5 Hz. The electrolyte resistance is shown by higher frequency Nyquist plot crossings on the Z'- axis (R_s). The charge transfer resistance (R_{ct}) at the electrode/electrolyte interface produced one
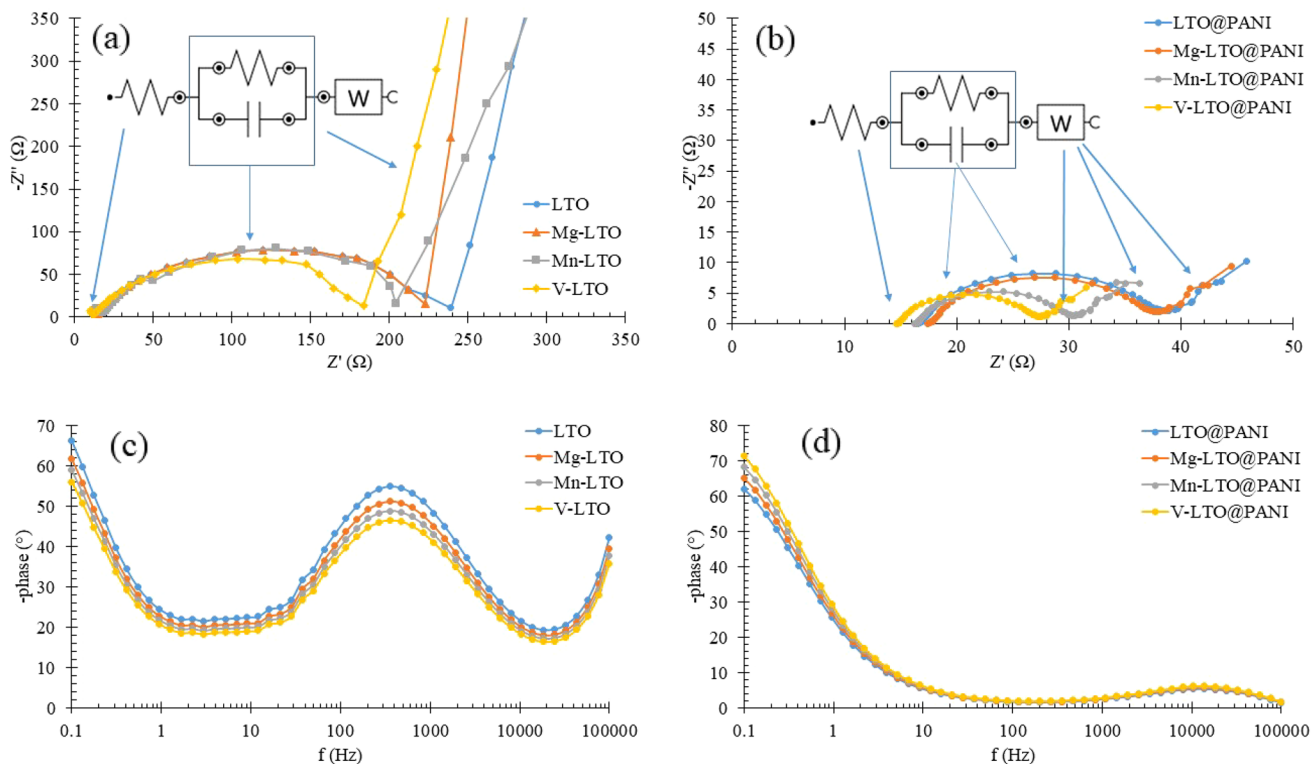

Fig. 9 Nyquist and bode modulus of the investigated samples

depressed semicircle to be seen at the high-frequency section [64], which is linked to the electrode's surface characteristic. [65]. There was also a spike at the lower frequencies, indicating supercapacitor behavior [78]. The electrode's Warburg impedance (W), also known as the diffusive resistance of Li^+ ions into the electrode, is indicated by the spike [24, 66]. To better understand the charge transfer mechanism at the electrolyte–electrode contact, the semicircle that appeared at higher frequencies is enlarged.

The diameter of the extrapolated semicircle on the $Z^/$-axis, which corresponds to the charge transfer resistance R_{ct}, is then used to compute its value at the electrolyte–electrode interface. Table 5 displays the results and shows that R_{ct} increases in either binary composite systems or LTO materials in the following order:

V-LTO < Mn-LTO < Mg-LTO < LTO.

This may be related to the decrease of dopants' ionic radius that facilitates the ionic diffusion of charge [70]. The main V (as V_2O_5), and Mn (as MnO_2) doped in LTO work as self-oxidizer for PANI formation. That gives V–N bond work as a bridge to ease the charge transfer between different polymer skeletons, beside the different V^{+5}, V^{+4}, V^{+3}, and V^{+2}, beside Mn^{+4}, Mn^{+3}, and Mn^{+2} (as shown in XPS) enhance the electrical conductivity and capacitive parameters.

The time constants (τ) of the capacitors were derived from the frequency (ω) coordinated at the maximum of the semicircle using the formula in Eq. (14) [67].

$$\tau = \frac{1}{\omega} \tag{14}$$

The results are listed in Table 5, which demonstrates that in τ increases in the order:

V-LTO > Mn-LTO > Mg-LTO > LTO in either LTO or their binary composite systems. The remarkable power responsiveness of the binary system is demonstrated by its small-time constants [68].

The Bode modulus of the phase angle is shown in Fig. 9. The graph implies that the phase angle (Φ) in the lower frequency (LF) region is $-65°$, but after PANI composing (Φ) in LF region is $-75°$ confirming the capacitive properties of the electrode ($\Phi = 0°$) for an ideal resistor and ($\Phi = 90°$) for an ideal supercapacitor in the low-frequency region [79, 80]. Figure 9 shows that the phase angles of the doped LTO samples increase after adding PANI, referring to increasing the capacitance behavior of the composite samples than that of single electrode material.[81].

4 Conclusions

In conclusion, a solid-state reaction was used to synthesize pure Mg–Mn–, and V-LTO nanoparticles. Composite samples of the pure and doped LTO and PANI were produced in situ chemical polymerization. The ac-electrical conductivity, dielectric constant, and electrochemical characteristics of the synthesized materials in a 1 M LiNO3 electrolyte solution were investigated to assess their potential as anode materials for energy storage. The electrochemical process was examined using charge–discharge (CD) and cyclic voltammetry (CV) techniques. The difference in dopants showed a pronounced effect on the electrical (σ_{ac}, $\varepsilon^/$, $\varepsilon^{//}$) and electrochemical properties (C_{sp}) of the single and composite samples. All the tested electrodes showed pseudo-capacitance behavior. Contributions from the pseudo-capacitance of PANI and the capacitance of LTO samples were visible in the composite materials. All the combined effects contributed to the fabricated electrodes' enhanced capacitance, energy density, and power density. The best performance was achieved for the V-LTO@PANI composite. The highest specific capacitance value of 218 F/g was attained at 1 A/g current density. The V-LTO@PANI electrode showed high cycling stability of 88.6% after 1000 cycles. At 1 A/g, a maximum energy density of 72.8 Wh/kg with a power density of 2430 W/kg was obtained. The tested materials, especially V-LTO@PANI, can be utilized as electrodes for energy storage devices because they are prepared using a simple and inexpensive synthetic method.

Declarations

References

1. A. Vlad, N. Singh, J. Rolland, S. Melinte, P.M. Ajayan, J.F. Gohy, Hybrid supercapacitor-battery materials for fast electrochemical charge storage. Sci. Rep. **4**, 1–7 (2014). https://doi.org/10.1038/srep04315

2. D. Chao, C. Zhu, X. Xia, J. Liu, X. Zhang, J. Wang, P. Liang, J. Lin, H. Zhang, Z.X. Shen, H.J. Fan, Graphene quantum dots coated VO2 arrays for highly durable electrodes for Li and Na Ion batteries. Nano Lett. **15**, 565–573 (2014). https://doi.org/10.1021/nl504038s

3. M. Chen, D. Chao, J. Liu, J. Yan, B. Zhang, Y. Huang, J. Lin, Z.X. Shen, Rapid pseudocapacitive sodium-ion response induced by 2D ultrathin tin monoxide nanoarrays. Adv. Funct. Mater. **27**, 1–8 (2017). https://doi.org/10.1002/adfm.201606232

4. S.L. Candelaria, Y. Shao, W. Zhou, X. Li, J. Xiao, J.G. Zhang, Y. Wang, J. Liu, J. Li, G. Cao, Nanostructured carbon for energy storage and conversion. Nano Energy **1**, 195–220 (2012). https://doi.org/10.1016/j.nanoen.2011.11.006

5. J. Duay, M. Kelly, T.N. Lambert, Evaluation of a ceramic separator for use in rechargeable alkaline Zn/MnO2 batteries. J. Power Sources. **395**, 430–438 (2018). https://doi.org/10.1016/j.jpowsour.2018.05.072

6. D. Zhao, Y. Wang, Y. Zhang, High-performance Li-ion batteries and super- capacitors based on 1-D. Nano-Micro Lett. **3**, 62–71 (2011)

7. M.D. Stoller, S. Park, Y. Zhu, J. An, R.S. Ruoff, Graphene-based ultracapacitors. Nano Lett. **8**, 3498–3502 (2008). https://doi.org/10.1021/nl802558y

8. Q. Meng, K. Cai, Y. Chen, L. Chen, Research progress on conducting polymer based supercapacitor electrode materials. Nano Energy **36**, 268–285 (2017). https://doi.org/10.1016/j.nanoen.2017.04.040

9. J. Zhou, J. Yu, L. Shi, Z. Wang, H. Liu, B. Yang, C. Li, C. Zhu, A conductive and highly deformable all-pseudocapacitive composite paper as supercapacitor electrode with improved areal and volumetric capacitance. Small **1803786**, 1–9 (2018). https://doi.org/10.1002/smll.201803786

10. A. Elmouwahidi, E. Bailón-garcía, A.F. Pérez-cadenas, N. Fernández-sáez, F. Carrasco-marín, Development of vanadium-coated carbon microspheres : electrochemical behavior as electrodes for supercapacitors. Adv. Funct. Mater. **1802337**, 1–9 (2018). https://doi.org/10.1002/adfm.201802337

11. Y.S. Lee, Y.K. Sun, K.S. Nahm, Synthesis of spinel LiMn2O4 cathode material prepared by an adipic acid-assisted sol-gel method for lithium secondary batteries. Solid State Ionics **109**, 285–294 (1998). https://doi.org/10.1016/s0167-2738(98)00085-x

12. B.J. Hwang, C.Y. Wang, M.Y. Cheng, R. Santhanam, Structure, morphology, and electrochemical investigation of LiMn2O4 thin film cathodes deposited by radio frequency sputtering for lithium microbatteries. J. Phys. Chem. C. **113**, 11373–11380 (2009). https://doi.org/10.1021/jp810881d

13. T.F. Yi, H. Liu, Y.R. Zhu, L.J. Jiang, Y. Xie, R.S. Zhu, Improving the high rate performance of Li 4Ti 5O 12 through divalent zinc substitution. J. Power Sources **215**, 258–265 (2012). https://doi.org/10.1016/j.jpowsour.2012.04.080

14. T. Yi, B. Chen, H. Shen, R. Zhu, A. Zhou, H. Qiao, Spinel Li4Ti5-xZrxO12 (0 ≤ x ≤ 0.25) materials as high-performance anode materials for lithium-ion batteries. J. Alloys Compd. **558**, 11–17 (2013). https://doi.org/10.1016/j.jallcom.2013.01.018

15. H. Jung, N. Venugopal, B. Scrosati, Y. Sun, A high energy and power density hybrid supercapacitor based on an advanced. J. Power Sources **221**, 266–271 (2013). https://doi.org/10.1016/j.jpowsour.2012.08.039

16. H. Yu, X. Zhang, A.F. Jalbout, X. Yan, X. Pan, H. Xie, R. Wang, High-rate characteristics of novel anode Li4Ti5O12/polyacene materials for Li-ion secondary batteries. Electrochim. Acta **53**, 4200–4204 (2008). https://doi.org/10.1016/j.electacta.2007.12.052

17. K. Mukai, K. Ariyoshi, T. Ohzuku, Comparative study of Li[CrTi]O4, Li[Li1/3Ti5/3]O4 and Li1/2Fe1/2[Li1/2Fe1/2Ti]O4 in non-aqueous lithium cells. J. Power Sources **146**, 213–216 (2005). https://doi.org/10.1016/j.jpowsour.2005.03.019

18. R. Bernhard, S. Meini, H.A. Gasteiger, On-line Electrochemical mass spectrometry investigations on the gassing behavior of Li4Ti5O12 electrodes and Its origins. J. Electrochem. Soc. **161**, A497–A505 (2014). https://doi.org/10.1149/2.013404jes

19. F. Li, M. Zeng, J. Li, H. Xu, Preparation and electrochemical performance of Mg-doped Li4Ti5O12 nanoparticles as anode materials for lithium-ion batteries. Int. J. Electrochem. Sci. **10**, 10445–10453 (2015)

20. H. Song, T.G. Jeong, S.W. Yun, E.K. Lee, S.A. Park, Y.T. Kim, An upper limit of Cr-doping level to Retain Zero-strain characteristics of Li4Ti5O12 anode material for Li-ion batteries. Sci. Rep. (2017). https://doi.org/10.1038/srep43335

21 E. Zhang, H. Zhang, Preparation and electrochemical properties of carbon-coated Li4Ti5O12 anode materials for Lithium Ion batteries. Int. J. Electrochem. Sci. **13**, 12380–12390 (2018). https://doi.org/10.20964/2018.12.74

22. X. Li, M. Qu, Z. Yu, Structural and electrochemical performances of Li4Ti5-xZrxO12 as anode material for lithium-ion batteries. J. Alloys Compd. **487**, 12–17 (2009). https://doi.org/10.1016/j.jallcom.2009.07.176

23. B.G. Lee, J.R. Yoon, Preparation and characteristics of Li4Ti5O12 anode material for hybrid supercapacitor. J. Electr. Eng. Technol. **7**, 207–211 (2012). https://doi.org/10.1016/j.cap.2013.04.002

24. E. Kang, Y.S. Jung, G.H. Kim, J. Chun, U. Wiesner, A.C. Dillon, J.K. Kim, J. Lee, Highly improved rate capability for a lithium-ion battery nano-Li4Ti5O12 negative electrode via carbon-coated mesoporous uniform pores with a simple self-assembly method. Adv. Funct. Mater. **21**, 4349–4357 (2011). https://doi.org/10.1002/adfm.201101123

25. L. Yang, L. Gao, Li4Ti5O12/C composite electrode material synthesized involving conductive carbon precursor for Li-ion battery. J. Alloys Compd. **485**, 93–97 (2009). https://doi.org/10.1016/j.jallcom.2009.05.151

26. H. Narayan, H. Alemu, E. Iwuoha, Synthesis, characterization and conductivity measurements of polyaniline and polyaniline/fly-ash composites. Phys. Status Solidi Appl. Mater. Sci. **203**, 3665–3672 (2006). https://doi.org/10.1002/pssa.200622304

27. S.K. Meher, P. Justin, G.R. Rao, Microwave-mediated synthesis for improved morphology and pseudocapacitance performance of nickel oxide. ACS Appl. Mater. Interfaces **3**, 2063–2073 (2011). https://doi.org/10.1021/am200294k

28. M. Chen, W. Li, X. Shen, G. Diao, Fabrication of core-shell α-Fe 2 O 3 @ Li 4 Ti 5 O 12 composite and Its application in the Lithium Ion batteries. ACS Appl. Mater. Interfaces **6**, 4514–4523 (2014). https://doi.org/10.1021/am500294m

29. B. Lee, J.R. Yoon, Preparation and characteristics of Li4Ti5O12 with various dopants as anode electrode for hybrid supercapacitor. Curr. Appl. Phys. **13**, 1350–1353 (2013). https://doi.org/10.1016/j.cap.2013.04.002

30. R. Dominko, M. Gaberscek, M. Bele, D. Mihailovic, J. Jamnik, Carbon nanocoatings on active materials for Li-ion batteries. J.

Eur. Ceram. Soc. **27**, 909–913 (2007). https://doi.org/10.1016/j.jeurceramsoc.2006.04.133

31. Q. Wu, Y. Xu, Z. Yao, A. Liu, G. Shi, Supercapacitors based on flexible graphene/polyaniline nanofiber composite films. ACS Nano **4**, 1963–1970 (2010). https://doi.org/10.1021/nn1000035

32. H. Wang, J. Lin, Z.X. Shen, Polyaniline (PANi) based electrode materials for energy storage and conversion. J. Sci. Adv. Mater. Devices. **1**, 225–255 (2016). https://doi.org/10.1016/j.jsamd.2016.08.001

33. A.S. Adekunle, K.I. Ozoemena, Electron transfer behaviour of single-walled carbon nanotubes electro-decorated with nickel and nickel oxide layers. Electrochim. Acta. **53**, 5774–5782 (2008). https://doi.org/10.1016/j.electacta.2008.03.044

34. A.S. Adekunle, K.I. Ozoemena, Insights into the electro-oxidation of hydrazine at single-walled carbon-nanotube-modified edge-plane pyrolytic graphite electrodes electro-decorated with metal and metal oxide films. J. Solid State Electrochem. **12**, 1325–1336 (2008). https://doi.org/10.1007/s10008-008-0539-x

35. R. Younesi, G.M. Veith, P. Johansson, K. Edström, T. Vegge, Lithium salts for advanced lithium batteries: Li-metal, Li-O2, and Li-S. Energy Environ. Sci. **8**, 1905–1922 (2015). https://doi.org/10.1039/c5ee01215e

36. K.F. Qasim, M.A. Mousa, Effect of oxidizer on PANI for producing BaTiO3@PANI perovskite composites and their electrical and electrochemical properties. J. Inorg. Organomet. Polym. Mater. **32**, 3093–3105 (2022). https://doi.org/10.1007/s10904-022-02335-8

37. K.F. Qasim, M.A. Mousa, Electrical and dielectric properties of self-assembled polyaniline on barium sulphate surface. Egypt. J. Pet. **30**, 9–19 (2021). https://doi.org/10.1016/j.ejpe.2021.09.001

38. M. Khairy, K. Faisal, M.A. Mousa, High-performance hybrid supercapacitor based on pure and doped Li4Ti5O12 and graphene. J. Solid State Electrochem. **21**, 873–882 (2017). https://doi.org/10.1007/s10008-016-3433-y

39. A. Laumann, Novel routes to Li4Ti5O12 spinel: Characterization and phase relations, Fakultät für Geowissenschaften der Ludwig–Maximilians–Universität München, 2010.

40. Y.Q. Jia, Crystal radii and effective ionic radii of the rare earth ions. J. Solid State Chem. **95**, 184–187 (1991). https://doi.org/10.1016/0022-4596(91)90388-X

41. R.D. Shannon, Revised effective ionic radii and systematic studies of interatomie distances in halides and chaleogenides. Acta Crystallogr. **32**, 751 (1976). https://doi.org/10.1023/A:1018927109487

42. M.A. Gabal, Synthesis, characterization and electrical conductivity of polyaniline-Mn0.8Zn0.2Fe2O4 nano-composites. Int. J. Electrochem. Sci. **11**, 4526–4538 (2016). https://doi.org/10.20964/2016.06.20

43. Heryanto, B. Abdullah, D. Tahir, Mahdalia, Quantitative analysis of X-Ray diffraction spectra for determine structural properties and deformation energy of Al, Cu and Si. J. Phys. Conf. Ser. **1317**, 012052 (2019). https://doi.org/10.1088/1742-6596/1317/1/012052

44. Z. Durmus, A. Baykal, H. Kavas, H. Szeri, Preparation and characterization of polyaniline (PANI)-Mn3O4 nanocomposite. Phys. B Condens. Matter. **406**, 1114–1120 (2011). https://doi.org/10.1016/j.physb.2010.12.059

45. N. Ahmed, M. Ramadan, W.M.A. El, Non-precious co-catalysts boost the performance of TiO2 hierarchical hollow mesoporous spheres in solar fuel cells. Int. J. Hydrogen Energy. **43**, 21219–21230 (2018). https://doi.org/10.1016/j.ijhydene.2018.10.012

46. J. Wang, Y. Zhou, T. Liao, Z. Lin, Trend in crystal structure of layered ternary T-Al-C carbides T=Sc, Ti, V, Cr, Zr, Nb, Mo, Hf, W and Ta). J. Mater. Res. **22**, 2685–2690 (2007). https://doi.org/10.1557/jmr.2007.0366

47. H. Ge, N. Li, D. Li, C. Dai, D. Wang, Study on the theoretical capacity of spinel lithium titanate induced by low-potential intercalation. J. Phys. Chem. C. **113**, 6324–6326 (2009). https://doi.org/10.1021/jp9017184

48. J. Haetge, P. Hartmann, K. Brezesinski, J. Janek, T. Brezesinski, Ordered large-pore mesoporous Li4Ti5O12 spinel Thin film electrodes with nanocrystalline framework for high rate rechargeable lithium batteries: relationships among charge storage, electrical conductivity, and nanoscale structure. Chem. Mater. **23**, 4384–4393 (2011). https://doi.org/10.1021/cm202185y

49. A. Osonkie, V. Lee, P. Chukwunenye, T. Cundari, J. Kelber, Plasma modification of vanadium oxynitride surfaces: characterization by in situ XPS experiments and DFT calculations. J. Chem. Phys. (2020). https://doi.org/10.1063/5.0027996

50. E. Hryha, E. Rutqvist, L. Nyborg, Stoichiometric vanadium oxides studied by XPS. Surf. Interface Anal. **44**, 1022–1025 (2012). https://doi.org/10.1002/sia.3844

51. G. Silversmit, D. Depla, H. Poelman, G.B. Marin, R. De Gryse, An XPS study on the surface reduction of V2O5 (001) induced by Ar+ ion bombardment. Surf. Sci. **600**, 3512–3517 (2006). https://doi.org/10.1016/j.susc.2006.07.006

52. G. Silversmit, D. Depla, H. Poelman, G.B. Marin, R. De Gryse, Determination of the V2p XPS binding energies for different vanadium oxidation states (V5+ to V0+). J. Electron Spectros. Relat. Phenomena. **135**, 167–175 (2004). https://doi.org/10.1016/j.elspec.2004.03.004

53. J. Mendialdua, R. Casanova, Y. Barbaux, XPS studies of V2O5, V6O13, VO2 and V2O3. J. Electron Spectros. Relat. Phenomena. **71**, 249–261 (1995)

54. M. Ding, G.E. Cutsail, D. Aravena, M. Amoza, M. Rouzières, P. Dechambenoit, Y. Losovyj, M. Pink, E. Ruiz, R. Clérac, J.M. Smith, A low spin manganese(IV) nitride single molecule magnet. Chem. Sci. **7**, 6132–6140 (2016). https://doi.org/10.1039/c6sc01469k

55. J. Feng, S. Tong, Y. Tong, G. Li, Pt-like hydrogen evolution Electrocatalysis on PANI / CoP hybrid nanowires by weakening the shackles of hydrogen ions on the surfaces of catalysts Pt-like hydrogen evolution electrocatalysis on PANI/CoP hybrid nanowires by weakening the shackles of hydr. J. Am. Chem. Soc. **140**, 5118 (2018). https://doi.org/10.1021/jacs.7b12968

56. I. Galesic, B.O. Kolbesen, Characterization of transition metal nitride formation in rapid thermal processing (RTP), fresenius. J. Anal. Chem. **365**, 199–202 (1999). https://doi.org/10.1007/s002160051472

57. B. Sreedhar, M. Sairam, D.K. Chattopadhyay, P.P. Mitra, D.V. Mohan Rao, Thermal and XPS studies on polyaniline salts prepared by inverted emulsion polymerization. J. Appl. Polym. Sci. **101**, 499–508 (2006). https://doi.org/10.1002/app.23301

58. S. Zhuk, S. Siol, Chemical state analysis of reactively sputtered zinc vanadium nitride: the auger parameter as a tool in materials design. Appl. Surf. Sci. **601**, 154172 (2022). https://doi.org/10.1016/j.apsusc.2022.154172

59. E.A. Kamar, K.F. Qasim, M.A. Mousa, Supercapacitor and oxygen evolution reaction performances based on rGO and Mn2V2O7 nanomaterials. Electrochim. Acta **430**, 141106 (2022). https://doi.org/10.1016/j.electacta.2022.141106

60. S. Ganapathy, M. Wagemaker, Nanosize storage properties in spinel Li4Ti5O12 explained by anisotropic surface lithium insertion. ACS Nano **6**, 8702–8712 (2012). https://doi.org/10.1021/nn302278m

61. M. Khairy, W.A. Bayoumy, K. Faisal, E.E. Elshereafy, M.A. Mousa, Electrical and electrochemical behavior of binary Li4Ti5O12–polyaniline composite. J. Inorg. Organomet. Polym. Mater. **30**, 3158–3169 (2020). https://doi.org/10.1007/s10904-020-01478-w

62. K.F. Qasim, W.A. Bayoumy, M.A. Mousa, Electrical and electrochemical studies of core–shell structured nanorods of LiMn2O4@PANI composite. J. Mater. Sci. Mater.

Electron. **31**, 19526–19540 (2020). https://doi.org/10.1007/s10854-020-04482-5

63. A.E. Etman, A.M. Ibrahim, F.A.M. Darwish, K.F. Qasim, Journal of industrial and engineering chemistry A 10 years-developmental study on conducting polymers composites for supercapacitors electrodes : a review for extensive data interpretation. J. Ind. Eng. Chem. **122C**, 27–45 (2023). https://doi.org/10.1016/j.jiec.2023.03.008

64 Fei Gao, Xiao Li, Zhanyu Li, Jianling Li, Yuguang Zhaoa, Kai Yang, Structure and electrochemical properties of Sm-doped Li4Ti5O12 as anode material for lithium-ion batteries. RSC Adv. **6**, 15492–15500 (2016)

65. Y. Purwamargapratala et al., Synthesis of Li4Ti5O12-Sn by ultrasonic method as anode materials for lithium ion battery. IOP Conf. Ser. Mater. Sci. Eng. **432**, 432 (2018)

66. S.M. Ebrahim, Fabrication of Schottky diode based on Zn electrode and polyaniline doped with 2-acrylamido-2-methyl-1-propanesulfonic acid sodium salt. J. Polym. Res. **16**, 481–487 (2009). https://doi.org/10.1007/s10965-008-9251-x

67. A.S. Roy, S.G. Hegde, A. Parveen, Synthesis, characterization, AC conductivity, and diode properties of polyaniline-CaTiO3 composites. Polym. Adv. Technol. **25**, 130–135 (2014). https://doi.org/10.1002/pat.3214

68. Z.Y. Yang, Y.F. Zhao, Q.Q. Xiao, Y.X. Zhang, L. Jing, Y.M. Yan, K.N. Sun, Controllable growth of CNTs on graphene as high-performance electrode material for supercapacitors. ACS Appl. Mater. Interfaces. **6**, 8497–8504 (2014). https://doi.org/10.1021/am501362g

69. Z.G. Shiquan Hong, Xiaobin Huang, Hong Liu, In situ chemical synthesis of MnO2/HMCNT nanocomposite with a uniquely developed three-dimensional open porous architecture for supercapacitors. J. Inorg. Organomet. Polym. Mater. **29**, 1587–15960 (2019)

70. X. Pu, D. Zhao, C. Fu, Z. Chen, S. Cao, C. Wang, Y. Cao, Understanding and calibration of charge storage mechanism in cyclic voltammetry curves. Angew. Chemie - Int. Ed. **60**, 21310–21318 (2021). https://doi.org/10.1002/anie.202104167

71. K. Zaghib, M. Simoneau, M. Armand, M. Gauthier, Electrochemical study of Li4Ti5O12 as negative electrode for Li-ion polymer rechargeable batteries. J. Power Sources. **81–82**, 300–305 (1999). https://doi.org/10.1016/S0378-7753(99)00209-8

72. M. Wilkening, R. Amade, W. Iwaniak, P. Heitjans, Ultraslow Li diffusion in spinel-type structured Li4Ti5O12- a comparison of results from solid state NMR and impedance spectroscopy. Phys. Chem. Chem. Phys. **9**, 1239–1246 (2007). https://doi.org/10.1039/b616269j

73. L. Wang, Y. Ye, X. Lu, Z. Wen, Z. Li, H. Hou, Y. Song, Hierarchical nanocomposites of polyaniline nanowire arrays on reduced graphene oxide sheets for supercapacitors. Sci. Rep. **3**, 1–9 (2013). https://doi.org/10.1038/srep03568

74. Z. Neisi, Z. Ansari-Asl, A.S. Dezfuli, Polyaniline/Cu(II) metal-organic frameworks composite for high performance supercapacitor electrode. J. Inorg. Organomet. Polym. Mater. **29**, 1838–1847 (2019). https://doi.org/10.1007/s10904-019-01145-9

75. M. Ciszewski, A. Mianowski, P. Szatkowski, G. Nawrat, J. Adamek, Reduced graphene oxide–bismuth oxide composite as electrode material for supercapacitors. Ionics (Kiel). **21**, 557–563 (2014). https://doi.org/10.1007/s11581-014-1182-4

76. S. Kalasina, N. Phattharasupakun, T. Maihom, V. Promarak, T. Sudyoadsuk, J. Limtrakul, M. Sawangphruk, Novel hybrid energy conversion and storage cell with photovoltaic and supercapacitor effects in ionic liquid electrolyte. Sci. Rep. **8**, 1–11 (2018). https://doi.org/10.1038/s41598-018-30707-z

77. Y. Shao, M.F. El-Kady, J. Sun, Y. Li, Q. Zhang, M. Zhu, H. Wang, B. Dunn, R.B. Kaner, Design and mechanisms of asymmetric supercapacitors. Chem. Rev. **118**, 9233–9280 (2018). https://doi.org/10.1021/acs.chemrev.8b00252

78. M. Khairy, W.A. Bayoumy, K.F. Qasim, E. El-Shereafy, M.A. Mousa, Ternary V-doped Li4Ti5O12-polyaniline-graphene nanostructure with enhanced electrochemical capacitance performance. Mater. Sci. Eng. B Solid-State Mater. Adv. Technol. **271**, 115312 (2021). https://doi.org/10.1016/j.mseb.2021.115312

79. N.K. Sidhu, A.C. Rastogi, Bifacial carbon nanofoam-fibrous PEDOT composite supercapacitor in the 3-electrode configuration for electrical energy storage. Synth. Met. **219**, 1–10 (2016). https://doi.org/10.1016/j.synthmet.2016.04.012

80 K. Adams, J. Mallows, T. Li, D. Kampouris, J.H.J. Thijssen, N. Robertson, Cs3Bi2I9 as high-performance electrode material achieving high capacitance and stability in an economical supercapacitor. J. Phys. Energy (2019). https://doi.org/10.1088/2515-7655/ab22d7

81. R. Rajalakshmi, K.P. Remya, C. Viswanathan, N. Ponpandian, Enhanced electrochemical activities of morphologically tuned MnFe2O4 nanoneedles and nanoparticles integrated on reduced graphene oxide for highly efficient supercapacitor electrodes. Nanoscale Adv. **3**, 2887–2901 (2021). https://doi.org/10.1039/d1na00144b

Khaled Faisal Qasim is an Assistant Professor at Chemistry Department, Faculty of Science, Suez University, Suez, Egypt. I have 9 articles indexed in scopus with expertise of electrochemistry, solid state chemistry, energy storage, and composites.

Mahmoud Ahmed Mousa is a Professor at Chemistry Department, Faculty of Science, Benha University, Benha, Egypt. He has over 100 articles indexed in scopus with expertise of solid state chemistry, Kinetics, energy storage, and radio chemistry.

⏁ Springer

Terms and Conditions

Springer Nature journal content, brought to you courtesy of Springer Nature Customer Service Center GmbH ("Springer Nature").

Springer Nature supports a reasonable amount of sharing of research papers by authors, subscribers and authorised users ("Users"), for small-scale personal, non-commercial use provided that all copyright, trade and service marks and other proprietary notices are maintained. By accessing, sharing, receiving or otherwise using the Springer Nature journal content you agree to these terms of use ("Terms"). For these purposes, Springer Nature considers academic use (by researchers and students) to be non-commercial.

These Terms are supplementary and will apply in addition to any applicable website terms and conditions, a relevant site licence or a personal subscription. These Terms will prevail over any conflict or ambiguity with regards to the relevant terms, a site licence or a personal subscription (to the extent of the conflict or ambiguity only). For Creative Commons-licensed articles, the terms of the Creative Commons license used will apply.

We collect and use personal data to provide access to the Springer Nature journal content. We may also use these personal data internally within ResearchGate and Springer Nature and as agreed share it, in an anonymised way, for purposes of tracking, analysis and reporting. We will not otherwise disclose your personal data outside the ResearchGate or the Springer Nature group of companies unless we have your permission as detailed in the Privacy Policy.

While Users may use the Springer Nature journal content for small scale, personal non-commercial use, it is important to note that Users may not:

1. use such content for the purpose of providing other users with access on a regular or large scale basis or as a means to circumvent access control;

2. use such content where to do so would be considered a criminal or statutory offence in any jurisdiction, or gives rise to civil liability, or is otherwise unlawful;

3. falsely or misleadingly imply or suggest endorsement, approval , sponsorship, or association unless explicitly agreed to by Springer Nature in writing;

4. use bots or other automated methods to access the content or redirect messages

5. override any security feature or exclusionary protocol; or

6. share the content in order to create substitute for Springer Nature products or services or a systematic database of Springer Nature journal content.

In line with the restriction against commercial use, Springer Nature does not permit the creation of a product or service that creates revenue, royalties, rent or income from our content or its inclusion as part of a paid for service or for other commercial gain. Springer Nature journal content cannot be used for inter-library loans and librarians may not upload Springer Nature journal content on a large scale into their, or any other, institutional repository.

These terms of use are reviewed regularly and may be amended at any time. Springer Nature is not obligated to publish any information or content on this website and may remove it or features or functionality at our sole discretion, at any time with or without notice. Springer Nature may revoke this licence to you at any time and remove access to any copies of the Springer Nature journal content which have been saved.

To the fullest extent permitted by law, Springer Nature makes no warranties, representations or guarantees to Users, either express or implied with respect to the Springer nature journal content and all parties disclaim and waive any implied warranties or warranties imposed by law, including merchantability or fitness for any particular purpose.

Please note that these rights do not automatically extend to content, data or other material published by Springer Nature that may be licensed from third parties.

If you would like to use or distribute our Springer Nature journal content to a wider audience or on a regular basis or in any other manner not expressly permitted by these Terms, please contact Springer Nature at

onlineservice@springernature.com